Entrainment and budgets of heat, water vapor, and carbon dioxide in a convective boundary layer driven by time-varying forcing

Jianping Huang,[1,2] Xuhui Lee,[1] and Edward G. Patton[3]

Received 20 August 2010; revised 9 January 2011; accepted 14 January 2011; published 30 March 2011.

[1] A large-eddy simulation (LES) code is coupled with a land surface model to investigate the diurnal variation of the atmospheric boundary layer (ABL). The diurnal evolution of the ABL is driven by a time-varying incoming solar radiation. The results show that the domain average surface fluxes of sensible heat, water vapor, and carbon dioxide are smooth functions of time but the fluxes at any given surface grid point show random variations, especially the sensible heat flux. At the ABL top, the LES-resolved entrainment fluxes of these scalars also evolve with time and are not fixed fractions of their respective surface fluxes. Entrainment efficiency (the ratio of entrainment flux at z_i to $w_e\delta\varphi$, where z_i is the ABL height, w_e is entrainment velocity, and $\delta\varphi$ is the jump of scalar across the entrainment zone) is highest for CO_2 and lowest for sensible heat. The first-order jump condition model is very good approximation to simulated entrainment fluxes which are largely controlled by the vertical gradients of the scalars across the capping inversion. Our results suggest that over the range of geostrophic winds considered (0–5 m s^{-1}), neither the surface nor the entrainment flux reveals sensitivity to the geostrophic wind speed variations.

Citation: Huang, J., X. Lee, and E. G. Patton (2011), Entrainment and budgets of heat, water vapor, and carbon dioxide in a convective boundary layer driven by time-varying forcing, *J. Geophys. Res.*, *116*, D06308, doi:10.1029/2010JD014938.

1. Introduction

[2] Surface-atmosphere interactions and entrainment play a critical role in the diurnal evolution of the atmospheric boundary layer (ABL). ABL budget analysis provides constraints on evaluating the surface and entrainment fluxes at the regional scale and for assessing their influences on the ABL development [*Betts and Ball*, 1994; *Barr and Betts*, 1997]. Compared to surface fluxes, entrainment flux observations are relatively scarce. In addition, parameterization of the entrainment process is not satisfactory in many ABL models. Accurate quantification of entrainment fluxes and ABL budgets are essential for a better understanding the dynamic evolution of the ABL.

[3] The ABL budget analysis of sensible heat and water vapor has been conducted extensively through field experiments and mixed layer models. *Betts et al.* [1990, 1992] and *Grossman* [1992] used aircraft data from the First International Satellite Land Surface Climatology Project (ISLSCP) Field Experiment (FIFE) to analyze the ABL budgets of sensible heat and water vapor, and confirmed that the vertical flux divergence plays a major role in the time change of potential temperature (θ) and specific humidity (q) in the ABL. *Barr and Betts* [1997] utilized the radiosonde data collected during the 1994 field phase of the Boreal Ecosystem-Atmosphere Study (BOREAS) to estimate the mean mixed-layer budget of sensible and latent heat fluxes. More recently, *Vil¨ -Guerau de Arellano et al.* [2004] combined aircraft data with surface measurements from the 2002 International H_2O Project to investigate entrainment fluxes and the ABL CO_2 budget, where they showed that the ABL CO_2 budget is dominated by vegetation uptake and by ventilation processes associated with ABL growth. ABL budgets can also be examined using mixed layer models [*Betts*, 1973; *Carson*, 1973; *Tennekes*, 1973; *Betts*, 1992; *Betts and Ball* 1994; *Vil¨ -Guerau de Arellano et al.*, 2004]. Most observational and modeling studies are restricted to sensible heat and water vapor. CO_2 budget analysis has received much less attention so far, partly because of the lack of observational data and limited abilities of numerical models.

[4] Entrainment is a crucial process controlling the budget of heat, water vapor and CO_2 in the ABL. However, observational data on the entrainment flux is very limited, hindering the development of accurate parameterization of the entrainment process in numerical models. In an ABL budget analysis, the heat flux at the top of boundary layer is usually assumed to be a constant fraction of the surface flux. But there is no consensus as to the exact value for this entrainment-to-surface flux ratio. For buoyancy fluxes, a constant value (0.2) is considered to represent the entrainment-to-surface flux ratio for the equilibrium state developed in a linearly stratified atmospheric boundary layer

[1]School of Forestry and Environmental Studies, Yale University, New Haven, Connecticut, USA.
[2]Now at IMSG, Rockville, Maryland, USA.
[3]Mesoscale and Microscale Meteorology Division, National Center for Atmospheric Research, Boulder, Colorado, USA.

0148-0227/11/2010JD014938

[*Fedorovich et al.*, 2004] as it agrees with the findings of laboratory tank experiments [*Deardorff*, 1980] and with the calculations with the zero-order jump model (ZOM) [*Betts*, 1973; *Carson*, 1973; *Tennekes*, 1973; *Fedorovich et al.*, 2004]. But *Betts et al.* [1990, 1992] and *Betts and Ball* 1994] observed much higher values (0.44 ± 0.21) for the entrainment-to-surface heat flux ratio during the FIFE field campaigns. *Angevine* [1999] observed similarly high entrainment-to-surface flux ratios (0.47 ± 0.11) during the 1996 Flatland boundary layer experiments. This ratio may also increase significantly with increasing shear-induced turbulence or as the convective boundary layer (CBL) shifts from (to) neutral stability during the morning (evening) transition. In addition, entrainment at the top of ABL may vary in response to changes in surface forcing [*Angevine*, 2008] and to the lapse rate in the free atmosphere above the boundary layer [*Sorbjan*, 1996]. In the water vapor budget, the ratio of the entrainment flux at z_i to surface flux is very sensitive to the moisture profile in the CBL. The aircraft and tower observations of *Górska et al.* [2008] showed larger entrainment CO_2 flux magnitude in the morning (flux ratio > 1) and smaller in the afternoon (flux ratio < 1) than the vegetation uptake. The existence of a large entrainment CO_2 flux reprensents a major diffiuclty for inferring the surface CO_2 flux using ABL budget methods [*Cleugh and Grimmond*, 2001]. An accurate ABL budget analysis requires improved understanding of the different mechanisms controlling the entrainment fluxes among these scalars.

[5] LES is a tool well suited for investigating the entrainment process [*Sorbjan*, 1996; *Sullivan et al.*, 1998; *Fedorovich et al.*, 2004]. Using a refined vertical grid in the entrainment zone, *Sullivan et al.* [1998] found that coherent structures are the primary instigator of entrainment in a clear convective boundary layer in the range of $13.6 \leq R_i \leq 43.8$ (where R_i is a bulk Richardson number defined as $g\alpha \delta\theta z_i/w_*^2$, where g is the acceleration of gravity, α is the coefficient of thermal expansion, $\delta\theta$ the potential temperature jump across the entrainment zone, w_* the convective velocity, and z_i the ABL height). They showed that the normalized entrainment rate w_e/w_* ($w_e = d\langle z_i\rangle/dt$) varies as AR_i^{-1} with $A \approx 0.2$. *Fedorovich et al.* [2004] showed that this entrainment-to-surface flux ratio (A) is obtained if the ABL flow is at quasi-equilibrium and that parameters of the entrainment process are evaluated with the ZOM model. They further demonstrated that the normalized temperature entrainment rate follows a −1 power law relationship with R_i under neutrally stratified conditions ($R_i < 10$) and a −3/2 power law in strongly stratified conditions ($R_i > 10$). *Sun and Wang* [2008] further linked the two different power laws and discussed the effect of stratification in the free atmosphere on the entrainment process. These LES studies were restricted to heat fluxes. Entrainment fluxes of water vapor and CO_2 have not been investigated nearly as thoroughly.

[6] In this study, we used the National Center for Atmospheric Research (NCAR) LES coupled with a land-surface model (LSM) to perform the budget analysis of sensible heat, water vapor and CO_2. Most previous LES investigations simulate short "snapshots" of the ABL driven by a constant surface flux condition, raising the possibility that the entrainment flux is dependent on the prescribed surface fluxes and the initial profiles. To overcome this problem, we have coupled the LES with a LSM, which allows dynamic feedback between the surface fluxes, the ABL flow and the entrainment. A time-varying forcing (i.e., incoming solar radiation) drives the LES-LSM, simulating the daytime evolution of potential temperature, water vapor, and CO_2 in the ABL. The entrainment fluxes at the top of the planetary boundary layer (PBL) are resolved explicitly instead of being parameterized as in some ensemble ABL models.

[7] We also use the coupled LES-LSM to investigate factors that control the entrainment fluxes of heat, water vapor, and CO_2. Currently, the first-order jump model is widely used to estimate the entrainment rates and minimum buoyancy flux. *Sullivan et al.* [1998] utilized an LES to investigate the relationship between the entrainment rate and the Richardson number. In the present study, we use the time-varying LES-LSM simulations to evaluate the ZOM [*Lilly*, 1968], the first-order jump model (FOM) [*Betts*, 1974; *Sullivan et al.*, 1998], and extend the discussion to the general-structure model (GSM) with respect to entrainment flux parameterization for heat, water vapor and CO_2. We are also interested in factors controlling the vertical gradient of CO_2 across the capping inversion layer because determining the inversion jump of CO_2 may allow CO_2 entrainment flux estimation using conventional tower-based measurements.

[8] The remainder of the paper is organized in the following way: A brief description of the dynamically coupled LES-LSM model and the model configurations are presented in section 2. The temporal surface flux variations, vertical profiles of mean potential temperature, specific humidity and CO_2 mixing ratio, and their respective vertical flux profiles are analyzed in section 3. In section 4, the entrainment processes of the three scalars are examined using three different parameters: entrainment flux, inversion jump and relative entrainment efficiency. Section 5 examines the relative roles of the entrainment and surface fluxes in the time change of potential temperature, water vapor and CO_2 mixing ratio during the daytime evolution of the ABL.

2. Methodology

2.1. The Coupled LES-LSM Model

[9] The LES code used in this study was originally described by *Moeng* [1984] and has since undergone several stages of refinement [e.g., *Sullivan et al.*, 1996; *Patton et al.*, 2005; *Huang et al.*, 2008]. Recently, an LSM model [*Ronda et al.*, 2001] has been implemented into the LES by *Huang et al.* [2009] to study the surface-atmosphere interactions. In this coupled LES-LSM code, periodic boundary conditions are used in the horizontal directions, at the surface vertical velocity is zero and Monin-Obukhov similarity with empirical formula proposed by *Businger et al.* [1971] is used locally, and a radiation boundary condition [*Klemp and Durran*, 1983] is used at the upper boundary of the domain to minimize the impact of gravity waves. Pseudospectral and finite difference methods are used to calculate horizontal and vertical derivatives, respectively. *Spalart et al.*'s [1992] third-order Runge-Kutta scheme is employed for all fields in time and each time step is dynamically determined based on the Courant-Friedrichs-Lewy (CFL) number.

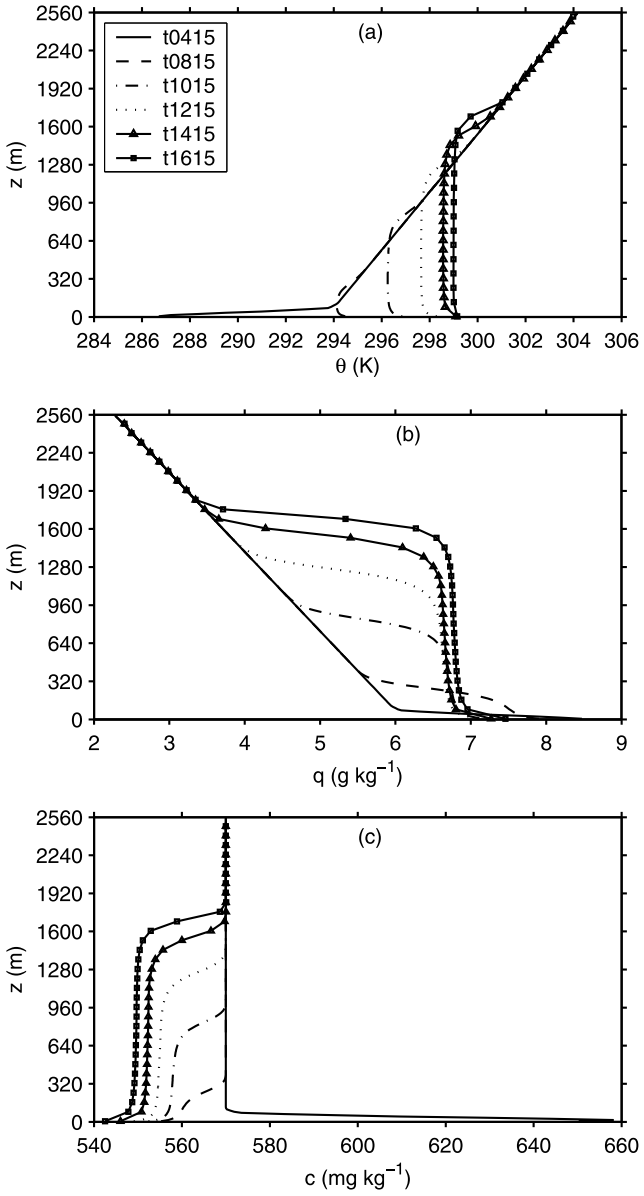

Figure 1. Vertical profiles of (a) potential temperature (θ), (b) specific humidity (q), and (c) CO_2 mixing ratio (c) for u_g = 5 m s^{-1}.

[10] In the coupled LES-LSM system, the LSM provides spatially and temporally varying surface heat, water vapor and CO_2 fluxes to the LES. The reference-height variables driving the LSM are provided by the LES at its lowest grid level. The LES simulates the evolution of the ABL, the instantaneous fields of velocity, potential temperature (θ), specific humidity (q), and CO_2 mixing ratio (c). Therefore, during these simulations both the surface and the entrainment fluxes are calculated directly.

2.2. Simulations With Time-Varying Forcing

[11] In the time-varying forcing simulations, the model domain consists of 256 × 256 × 256 grid cells with grid spacings of 40 m × 40 m × 10 m in the x, y, and z directions, respectively. Four simulations spanning four different imposed geostrophic wind speeds (u_g = 0, 1, 3, 5 m s^{-1}) are conducted. Initial θ and q profiles are specified according to composite sounding profiles collected at sunrise during the 1994 intensive field campaigns in the BOREAS southern study area (SSA, Figures 1a and 1b) [*Barr and Betts*, 1997]. *Barr and Betts* [1997] also reported the evolution of these profiles through the day, which are used to validate our LES results. The initial CO_2 profile consists of a shallow layer with a strong gradient of −2.8 mg kg^{-1} m^{-1} near the surface and a constant value of 570 mg kg^{-1} above (see Figure 1c).

[12] A time-varying incoming solar radiation is used to drive the dynamic evolution of the ABL [*Leuning et al.*, 1995],

$$S_0 = \tau_a S_c \sin\beta, \tag{1}$$

where τ_a is the atmospheric transmissivity of 0.84 representative of clear sky conditions, S_c is the extraterrestrial irradiance on a plane perpendicular to the Sun's rays, and β denotes solar zenith angle. The time variation of S_0 corresponds to the latitude of the BOREAS southern study area for a typical midsummer day under clear sky conditions (Figure 2). All simulations start at 0415 local standard time (LST) and last until 1615 LST. The incoming long-wave radiation flux density is parameterized according to the formulation of *Idso* [1981]. The emissivity of the earth's surface is assumed as a constant (0.97) throughout the simulations. To avoid turbulence collapse in the LES runs, a minimum S_0 of 130 W m^{-2} is imposed resulting in a slightly positive surface sensible heat flux of about 2 W m^{-2} between 0415 and 0615 LST (Figure 3). Initially, the surface is homogeneous throughout the domain, with constant soil moisture and biological parameters. Soil moisture is implicitly specified in the LSM by setting the photosynthetic capacity to a fraction of its maximum capacity (f_5 = 0.2) [*Huang et al.*, 2009].

2.3. Snapshot LES Simulations

[13] In two earlier studies, we performed snapshot LES simulations to investigate the flux imbalance problem and dissimilarity of scalar transport near the ground [*Huang et al.*, 2008, 2009]. In this current study, these previously

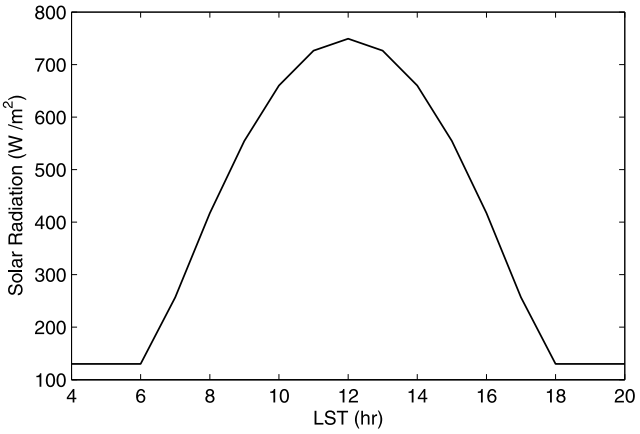

Figure 2. Solar radiation flux reaching the surface as a function of local standard time at latitude 53.73°N on day 250.

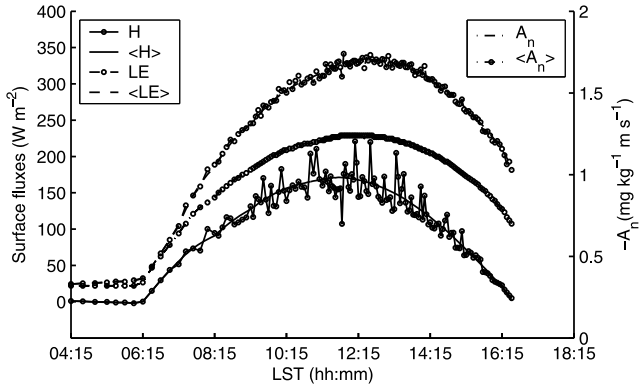

Figure 3. Temporal variations in sensible heat flux (H), latent heat flux (LE), and CO_2 flux (A_n) at the central point and averaged across the whole domain for u_g = 5 m s^{-1} (solid line, H; dashed line, LE; dash-dotted line, A_n; with circle, central point; without circle, domain average).

presented simulations are utilized to compare their entrainment statistics with those of the time-varying simulations discussed here. In these snapshot simulations, the initial profiles are prescribed for a fully developed well-mixed CBL. The simulations start with random divergence-free white noise added to the initial fields since the fluid is assumed impressible and there is no subsidence in our simulations. Incoming solar radiation for these snapshot simulations is held fixed at 700 W m^{-2}. ABL statistics are computed for each simulated hour.

3. Characteristics of the Evolving ABL

3.1. Surface Fluxes

[14] Figure 3 shows the temporal variations in the surface sensible heat flux (H), latent heat flux (LE), and CO_2 flux (A_n) averaged over the $x - y$ directions of the domain and at the central grid point of the simulation domain with u_g = 5 m s^{-1}. Increasing u_g from 0 to 5 m s^{-1} changes the domain averaged fluxes slightly, increasing the midday H by 3.8%, decreasing LE by 1.0% and A_n by 0.9% (Table 1), and makes the flux values less variable with time (i.e., the standard deviation of the surface fluxes decreases with increasing u_g). The domain mean wind speed $\langle u^2 + v^2 \rangle^{0.5}$ at the first grid height shows a modest variation of 0.99–1.34 m s^{-1} and 2.52–2.71 m s^{-1} corresponding to u_g = 0 and 5 m s^{-1} during the midday. Strong surface friction (z_0 = 0.5 m) could partly account for this minor impact. We did an additional run with u_g = 15 m s^{-1}, and see increasing the midday H by 13.3%, decreasing LE by 4.0% and A_n by 5.3%. Our simulated midday surface sensible and latent heat fluxes are comparable to the values observed in the BOREAS SSA area (166 W m^{-2} for H and 185 W m^{-2} for LE [*Barr and Betts*, 1997]). As expected, the domain-averaged surface fluxes closely follow the diurnal incoming solar radiation pattern (Figure 3). The sensible and latent fluxes at the central grid point show fluctuations with time in response to the feedbacks of organized turbulent flow in the ABL [*Huang et al.*, 2009]. The largest fluctuations occur near noon when the convective turbulence is fully developed and turbulence intensity, as measured by $\langle TKE \rangle / \langle W_*^2 \rangle$ relating the magnitude of the turbulence kinetic energy (TKE) to the current forcing, is the strongest (data not shown). In comparison, the temporal fluctuation is not apparent in A_n. In the current LSM implementation, variations in photosynthesis at the subminute time scales are controlled by the surface temperature which is not sensitive to the turbulent motion in the ABL. The fluctuations at the central grid are typical of those at other grid points in the model domain.

3.2. Vertical Profiles of θ, q, and c

[15] The simulated vertical profiles of θ, q, and CO_2 mixing ratio (c) are shown in Figure 1. An u_g value of 5 m s^{-1} is used in the simulation, similar to the mean geostrophic wind observed at the BOREAS southern study area [*Barr and Betts*, 1997]. The time sequence presented in Figure 1 covers the period from 0415 LST to 1615 LST, at an interval of 2 h. The profiles at 0415 LST are the initial profiles. Each subsequent profile represents an average over 200 time steps (3~7 min) and across the entire horizontal domain. By 0815 LST, 2 h after sunrise, the strong surface inversion layer is replaced by a shallow CBL. With the strengthening of solar radiation, a typical CBL gradually develops. The ABL growth is rapid in the morning and relatively slow in the afternoon (Figure 1a). At 1615 LST, a well-mixed CBL height has reached 1700 m. The CBL is characterized by a typical three-layered structure, with a surface layer showing a large vertical θ gradient, a mixed layer in which θ is uniform, and an entrainment zone with inversion strength exceeding that of the overlying atmosphere. The specific humidity and CO_2 mixing ratio profiles evolve in response to their respective surface and entrainment fluxes. Their midday profiles also consist of three layers. At 1615 LST, the q value in the midboundary layer is 1.9 g kg^{-1} greater and c is 20.9 mg kg^{-1} lower than the initial value.

[16] The simulated boundary layer characteristics evolve in reasonable agreement with the observations reported by *Barr and Betts* [1997]. Figure 4 compares the simulated ABL height with the measurements from the 1994 intensive campaigns in the BOREAS southern study area [*Barr and Betts*, 1997]. Here the ABL height is defined as the height of the maximum potential temperature gradient. The same methodology was used to determine the ABL height using the sounding data from the 1994 BOREAS field experiment [*Barr and Betts*, 1997]. Generally good agreement is achieved. Good agreement is also seen between the θ profiles shown in Figure 1 and the observed profiles [*Barr and Betts*, 1997, Figure 2]. The simulated q profiles agree

Table 1. Dependence of Surface and Entrainment Flux on the Geostrophic Wind[a]

u_g, m s^{-1}	Temperature, K m s^{-1}		Specific Humidity, g kg^{-1} m s^{-1}		CO_2, mg g^{-1} m s^{-1}	
	Surface	Entrainment	Surface	Entrainment	Surface	Entrainment
0	0.105	−0.024	0.101	0.067	−1.13	−0.46
1	0.105	−0.023	0.101	0.068	−1.13	−0.47
3	0.107	−0.023	0.100	0.068	−1.12	−0.46
5	0.109	−0.023	0.100	0.068	−1.12	−0.47

[a]The flux values are averaged between 0900 and 1500 LST.

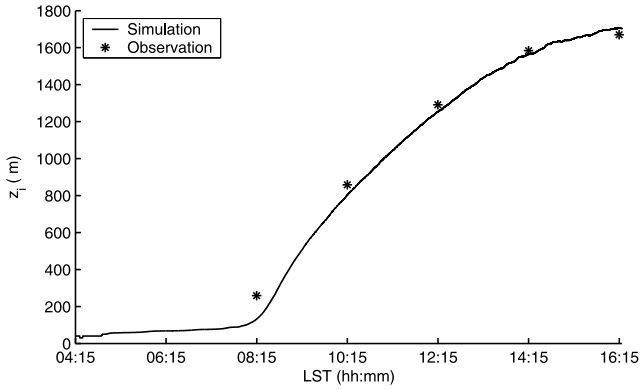

Figure 4. Comparison of simulated (solid line) with observed mixed-layer height (asterisks) for $u_g = 5$ m s^{-1}.

broadly with the observations except for two details. First, the simulated q profile is uniform with height in the mixed layer from 1015 LST onward whereas the observed q shows a slight vertical gradient. Second, the inversion jump of the modeled q is 3 g kg^{-1} at 1615 LST, roughly 1 g kg^{-1} higher than the observed jump value at that time. These discrepancies can be partly explained by the fact that our simulations only focus on the clear-sky CBL whereas the composite profiles derived from the soundings represent the mean situation of different boundary layer conditions including cloudy skies. Another potential factor causing this discrepancy is the local horizontal advection which may increase moisture in the lower part of atmospheric boundary layer over the BOREAS observational domain. However, the role of horizontal advection is not included in our simulations.

[17] *Lloyd et al.* [2001] found that without the inclusion of appreciable subsidence, their ABL budget model overestimates the growth of the CBL on a July afternoon over a mosaic landscape in central Siberia. No subsidence is included in our LES runs. The reasonably good agreement of the ABL growth (Figure 4) suggests either that subsidence is not an important factor when averaging over many ABL soundings that span a wide range of synoptic conditions or that other compensating mechanisms are not accounted for by our model.

3.3. Vertical Flux Profiles

[18] Figure 5 presents hourly- and domain-average profiles of vertical potential temperature, specific humidity and CO_2 mixing ratio fluxes for the same case as in Figure 1. Consistent with other LES studies [e.g., *Patton et al.*, 2005; *Huang et al.*, 2008, 2009], the vertical scalar flux profiles at any given time follow a linear relationship with height within the mixed layer, indicating that the linear relationship is the result of vertical mixing in the CBL despite the time-varying surface forcing. As expected, the heat flux at the top of the boundary layer (i.e., the entrainment flux) is of opposite sign to the surface heat flux. Both fluxes act to warm the ABL but the surface flux plays a larger role as the entrainment heat flux at z_i level is a small fraction (14 to 38%) of the surface flux (Figure 5a).

[19] The surface evapotranspiration is a moisture source whereas entrainment is a moisture sink for the ABL. The relative roles of entrainment versus surface water vapor flux in the time evolution of q in the ABL is determined by the ratio of the entrainment flux at z_i to surface water vapor flux (r_q): $r_q < 1$ corresponds to a temporal increase in q and $r_q > 1$ to a decrease in q (see Figures 1b and 5b). The flux ratio (r_q) is highly dependent on time of the day and to a lesser extent on the initial vertical profile prescribed in the LES simulations. In this study, r_q varies from 1.4 at 0815 LST to 0.5 at 1615 LST for the case with $u_g = 5$ m s^{-1}. r_q can be higher than 3.0 in the snapshot simulations [*Huang et al.*, 2009].

[20] During the period shown in Figure 5, the surface is a sink of CO_2 due to photosynthesis and entrainment process is a source of CO_2 in the ABL. Both fluxes are directed

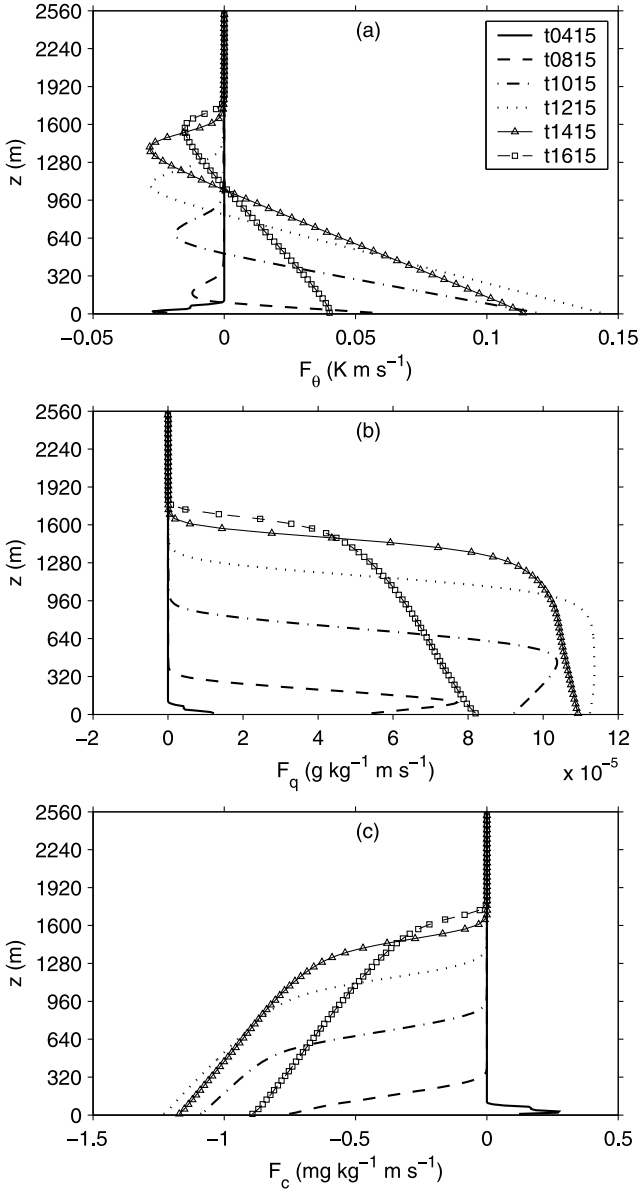

Figure 5. The same as Figure 3 but for (a) temperature flux, (b) specific humidity flux, and (c) CO_2 flux for $u_g = 5$ m s^{-1}.

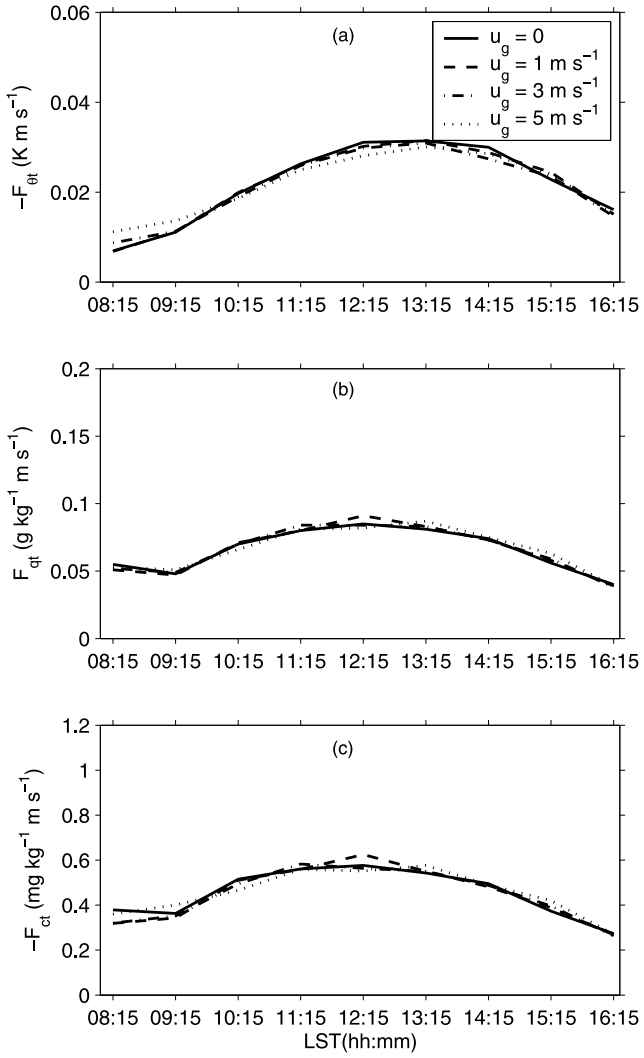

Figure 6. LES-resolved entrained fluxes of (a) heat, (b) water vapor, and (c) CO_2 (solid line, 0 m s^{-1}; dashed line, 1 m s^{-1}; dash-dotted line, 3 m s^{-1}; dotted line, 5 m s^{-1}).

downward (negative). The ratio of the entrainment flux at z_i to surface flux (r_c) varies from 0.5 to 0.3.

4. Entrainment Processes

4.1. Entrainment Flux

[21] In response to diurnally varying solar forcing, the boundary layer grows each day through entrainment, which exchanges heat, water vapor, CO_2 between the ABL and the free atmospheric layer. It is difficult to make direct measurement of entrainment fluxes. The entrainment buoyancy flux is typically assumed as a constant fraction of the surface flux in the ZOM [*Lilly*, 1968] or described as a function of the entrainment zone thickness in the FOM [*Betts*, 1974; *Sullivan et al.*, 1998]. In contrast, entrainment fluxes within the LES are explicitly calculated and are a result of the simulation.

[22] Figure 6 shows the time evolution of entrainment fluxes of heat, water vapor and CO_2 calculated with the LES for four different geostrophic wind conditions. The values shown here represent the domain- and hourly-averaged fluxes. Based on the study of *Sullivan et al.* [1998], a 10 m vertical resolution is fine enough to resolve the turbulence organized structure within the entrainment zone. The entrainment flux of heat follows a similar time variation pattern of the surface flux. Both entrainment fluxes of water vapor and CO_2 flux follow similar patterns but before 0915 LST are not sensitive to the surface fluxes. The geostrophic wind variations have negligible influence on the three entrainment fluxes (Table 1 and Figure 6). Therefore, for the atmospheric situations simulated here, the entrainment fluxes are more sensitive to the surface flux than to the geostrophic wind.

[23] We now use the LES results to evaluate several entrainment parameterizations. These parameterizations are based on the budget equation originally written for virtual potential temperature (neglecting radiation and mean vertical motion) [*Betts*, 1974, equation (2)] and are extended here to a general scalar φ (i.e., θ, q, and CO_2 mixing ratio c in this study),

$$\overline{\langle w''\varphi''\rangle}_{i,g} = \frac{d}{dt}((z_2 - z_i)\hat{\varphi}_{i2}) + \frac{dz_i}{dt}\varphi_i - \frac{dz_2}{dt}\varphi_2, \qquad (2a)$$

where $\langle\ \rangle$ denotes spatial averaging in the $x - y$ directions, overbar represents temporal averaging, double prime denotes fluctuation from the spatial average, $\overline{\langle w''\varphi''\rangle}_{i,g}$ represents the domain- and hourly-averaged entrainment flux at z_i and subscript g denotes GSM, z_i is the vertical position where buoyancy flux reaches the minimum value, z_2 is the vertical location where the buoyancy flux first goes to zero above the ABL height z_i, the height of z_2 is usually taken as the vertical location where the vertical flux reaches a prescribed fraction of the entrainment flux at z_i (Figure 7), φ_i and φ_2 are the scalar values at z_i and z_2, respectively, $\hat{\varphi}_{i2}$ is the average of φ between z_i and z_2, $\frac{d}{dt}$ is the derivative with respect to time (t). The readers are reminded that all the terms on the right side in equation (2a) represent horizontally averaged quantities and the angle brackets are omitted for simplicity. Our GSM is established in terms of the budget equation derived by *Betts* [1974, equation (2)]. As compared to the GSM of *Deardorff* [1979], the GSM discussed in this study

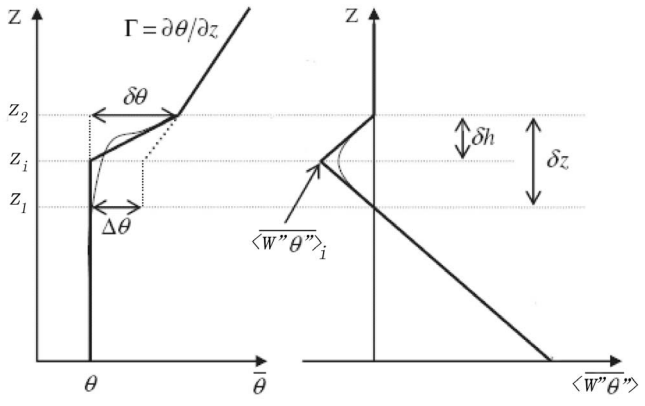

Figure 7. Sketch of entrainment zone structure for the general-structure model, first-order jump model, and zero-order jump model. Adapted from *Sun and Wang* [2008].

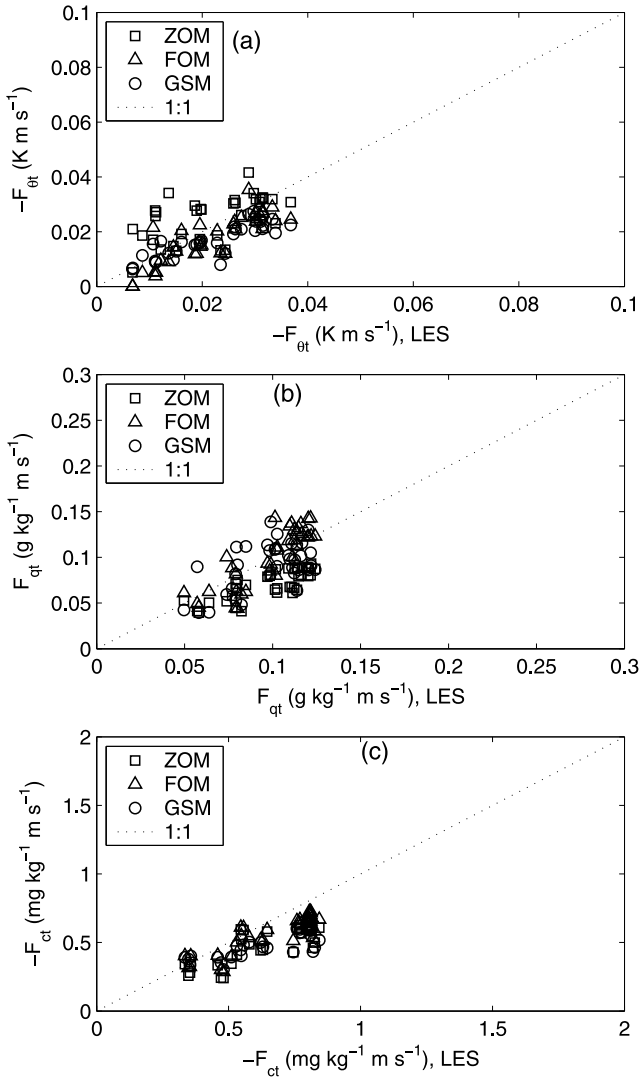

Figure 8. Comparison of LES-resolved entrainment fluxes with those of ZOM, FOM, and GSM in four different wind conditions for (a) temperature flux, (b) specific humidity flux, and (c) CO_2 flux.

has a relative simple form and is convenient for our discussion because we do not need to determine the integral shape factor in *Deardorff*'s [1979] formula (equation (30) in his study). In this study, our GSM framework assumes $\frac{dz_i}{dt} = \frac{dz_2}{dt} = w_e$, which means that the entrainment flux can be written as

$$\overline{\langle w''\varphi''\rangle}_{i,g} = \frac{\delta z}{2}\frac{d}{dt}\hat{\varphi}_{i2} + \frac{\hat{\varphi}_{i2}}{2}\frac{d}{dt}\delta z - w_e\delta\varphi_{i2}, \tag{2b}$$

where $\delta\varphi_{i2} = \varphi_2 - \varphi_i$, δz is the inversion-layer thickness ($\delta z = z_2 - z_1$) and $z_2 - z_i = \frac{\delta z}{2}$. *Betts* [1974] neglected the time change of the inversion thickness to further simplify equation (2b) into the FOM as follows:

$$\overline{\langle w''\varphi''\rangle}_{i,f} = -w_e\delta\varphi_{i2} + \frac{\delta z}{2}\frac{d}{dt}\hat{\varphi}_{i2} \tag{3a}$$

where $\overline{\langle w''\varphi''\rangle}_{i,f}$ denotes the entrainment flux at z_i calculated with the FOM and subscript f indicates FOM. If $\delta\varphi_{i2}$ is constant and $\delta\varphi_{12} = 2\delta\varphi_{i2}$, equation (3a) becomes

$$\overline{\langle w''\varphi''\rangle}_{i,f} = -\frac{w_e}{2}\left(\delta\varphi_{12} - \Gamma_{\varphi,1}\delta z\right) \tag{3b}$$

where $\Gamma_{\varphi,1}$ denotes the vertical gradient of scalar φ between z_i and z_2 (within entrainment zone), $\delta\varphi_{12}$ is the jump for the FOM across the entrainment zone and defined as the difference of φ between height z_1 where the flux $\overline{\langle w''\varphi''\rangle}_{i,z}$ reaches zero below z_i and height z_2 where the flux $\overline{\langle w''\varphi''\rangle}_{i,z}$ reaches zero above z_i (e.g., $\delta\theta$ illustrated by Figure 7). The jumps $\delta\varphi_{12}$ are similar to the potential temperature jump $\delta\theta$ defined by *Fedorovich et al.* [2004, Figure 1] and *Sun and Wang* [2008, Figure 1] but different from the one used by *Sullivan et al.* [1998]. In fact, our FOM (equation 3a) is very similar to equation (8) of *Sullivan et al.* [1998] if we consider $\delta\varphi_{12} = 2(\varphi_2 - \varphi_i)$ and $\delta z = 2(z_2 - z_i)$.

[24] On the other hand, ZOM expresses the entrainment flux at z_i [*Fedorovich et al.*, 2004]

$$\overline{\langle w''\varphi''\rangle}_{i,z} = -w_e\left(\delta\varphi_{12} - \Gamma_{\varphi,2}\delta h\right), \tag{4a}$$

where $\Gamma_{\varphi,2}$ is the vertical gradient of scalar in the free atmospheric layer (e.g., Γ illustrated by Figure 7) and $\delta h = z_2 - z_i$. The ZOM can be rewritten in a simplified form

$$\overline{\langle w''\varphi''\rangle}_{i,z} = -w_e\Delta\varphi \tag{4b}$$

where $\overline{\langle w''\varphi''\rangle}_{i,z}$ denotes the entrainment flux at z_i and calculated with ZOM with subscript z indicating ZOM, $\Delta\varphi$ is the jump of ZOM across the entrainment zone and defined as the difference between the value of extrapolation of the scalar profile from the free atmosphere down to z_i and the value at the bottom of the entrainment zone (Figure 7), similar to the one defined by *Fedorovich et al.* [2004] and *Sun and Wang* [2008]. The bottom of the entrainment zone is defined as the height where the flux $\overline{\langle w''\varphi''\rangle}_{i,z}$ reaches zero below z_i.

[25] In Figure 8, the entrainment fluxes of heat, water vapor and CO_2 simulated by the LES are compared with entrainment flux estimates based upon the ZOM, FOM and GSM. While the ZOM slightly underpredicts the magnitude of the entrainment fluxes at z_i, the FOM and GSM show very good agreement with the LES-resolved entrainment fluxes at z_i. It is worth noting that determining the zero-order scalar jump $\Delta\varphi$ is crucial to the parameterized entrainment fluxes. For example, the scalar jump calculated with $\Delta\varphi = \varphi_i - \varphi_1$ or $\Delta\varphi = \varphi_2 - \varphi_1$ may cause significant underprediction (overprediction) as compared to the LES-resolved entrainment fluxes. Our calculations suggest the ZOM is a good approximation to the entrainment fluxes at z_i if $\Delta\varphi = \varphi_2 - \varphi_1 - \Gamma_{2,\varphi}\delta h$ is utilized. The results are consistent with the findings of *Fedorovich et al.* [2004].

[26] Overall the FOM is a good approximation to parameterize the entrainment flux for the three scalars, and the ZOM is also a good approximation if the zero-order jump across the entrainment zone is calculated correctly. The performance of FOM suggests that the role of time change of the thickness of entrainment zone is negligible in the calculation of entrainment flux at z_i.

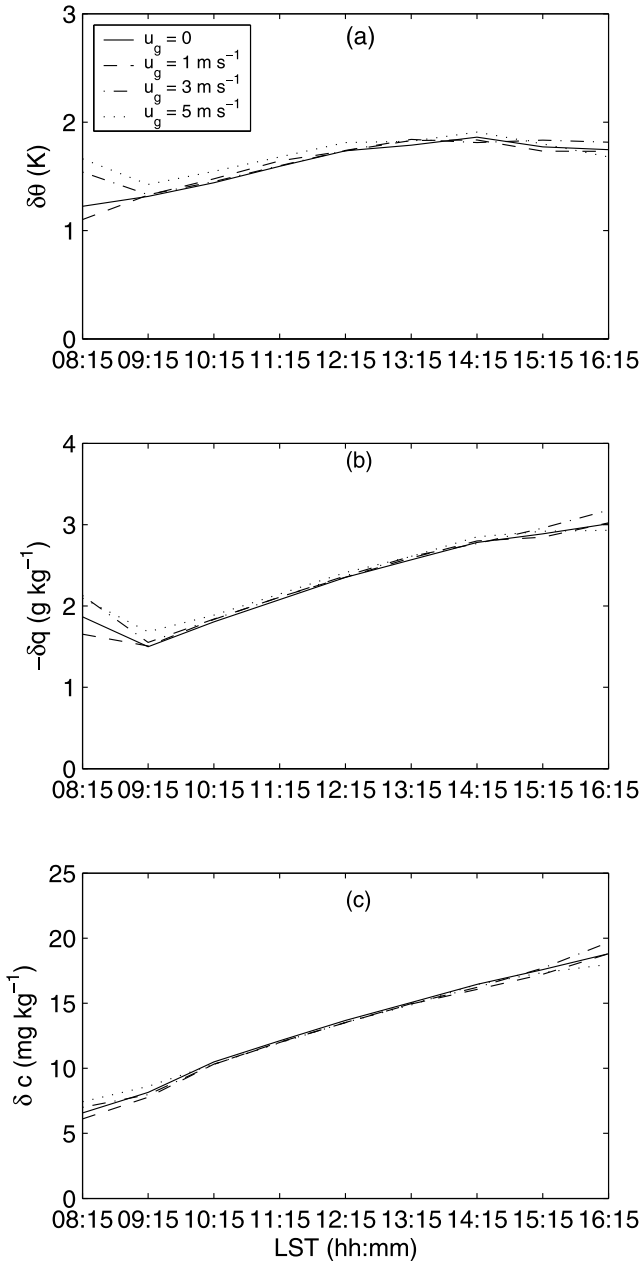

Figure 9. Temporal variations in the jump across the capping inversion of (a) potential temperature ($\delta\theta$), (b) specific humidity (δq), and (c) CO_2 mixing ratio (δc) for four geostrophic wind speeds.

4.2. Jumps of θ, q, and c Across the Capping Inversion

[27] The jumps of θ, q and c across the capping inversion, or differences in these scalar quantities between the free atmosphere and the mixed layer largely control the entrainment fluxes at the top of the ABL. The inversion jump of c, a critical parameter for inferring the surface CO_2 flux at the landscape scale from the time series of the CO_2 mixing ratios measured in the ABL [*Helliker et al.*, 2004; *Betts et al.*, 2004; *Lai et al.*, 2006; *Cleugh and Grimmond*, 2001], is rarely measured. Instead, it is sometimes taken as the difference between the tower-based measurement on land and the observation taken in the marine boundary layer, a proxy representing CO_2 mixing ratio in the free atmosphere, for the regional CO_2 flux calculations [*Chen et al.*, 2006], or is arbitrarily specified in snapshot LES studies [*Górska et al.*, 2008; *Huang et al.*, 2009]. In both snapshot and time-varying forcing simulations, the inversion jumps vary with the surface fluxes and the PBL growth. However, for the time-varying forcing cases, the surface fluxes evolve over time in response to the solar forcing and the entrainment. Thus the jump value in the current time-varying simulation is closer to the reality than the one calculated with the snapshot simulation.

[28] Figure 9 illustrates the evolution of the jumps of potential temperature, specific humidity and CO_2 mixing ratio ($\delta\theta$, δq, δc) derived from the time varying LES-LSM simulations. Here $\delta\theta$, δq, δc are calculated as the difference between the values at z_2 (the location where the vertical heat flux reaches zero above z_i; see Figure 7) and the value at z_1 (the location where the vertical heat flux reaches zero below z_i; see Figure 7). The $\delta\theta$ follows a similar temporal variation pattern of the surface heat flux, increasing quickly in the morning and then tending to slightly decrease in the afternoon, which indicates that surface flux plays a dominant role in the evolution of $\delta\theta$. In contrast, both $-\delta q$ and δc follow linear increasing trends. The changes in $\delta\theta$ and δq are consistent with the findings of *Vil¨-Guerau de Arellano et al.* [2004], but δc is different from their result in which dilution process is more important than ours and negative jumps are reported for the morning hours which results from different initial CO_2 profiles between the two investigations. The inversion jumps are insensitive to the geostrophic wind variations investigated here.

4.3. Relative Entrainment Efficiency

[29] The entrainment process can be further understood through the examination of the relative entrainment efficiency for heat (B_θ), water vapor (B_q), and CO_2 (B_c). In this study, we define the relative entrainment efficiency as

$$B_\theta = -\frac{\overline{\langle w''\theta''\rangle}_i}{w_e \delta\theta}, \tag{5a}$$

$$B_q = -\frac{\overline{\langle w''q''\rangle}_i}{w_e \delta q}, \tag{5b}$$

$$B_c = -\frac{\overline{\langle w''c''\rangle}_i}{w_e \delta c}, \tag{5c}$$

where $\delta\theta$, δq, and δc represent the jumps of θ, q, and c across the entire entrainment zone (as defined in section 4.2), and $\overline{\langle w''\theta''\rangle}_i$, $\overline{\langle w''q''\rangle}_i$, and $\overline{\langle w''c''\rangle}_i$ represent the hourly and domain-wide averaged LES-resolved entrainment fluxes at z_i.

[30] These coefficients can also be interpreted as the normalized entrainment fluxes or apparent diffusivities of the entrainment process. In equations (5a)–(5c), all the quantities on the right hand side are calculated directly from the LES simulations. In general, the entrainment efficiency is highest for CO_2 and lowest for temperature. In the time varying simulations, B_q and B_θ are higher in the morning and lower in the afternoon due to slower growth of the ABL

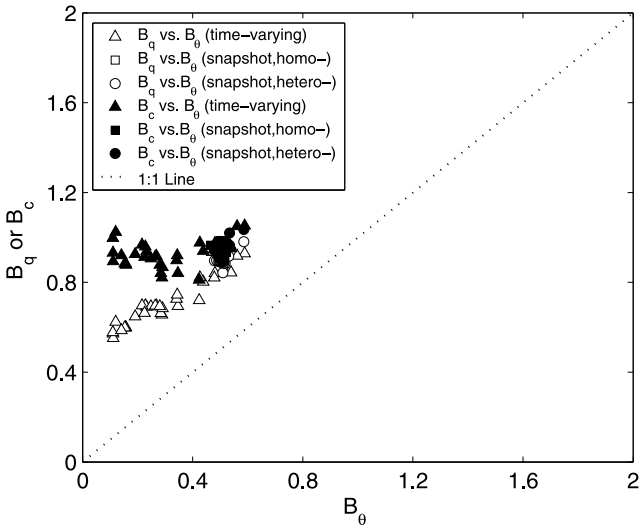

Figure 10. Comparison of relative entrainment efficiency of heat (B_θ), water vapor (B_q), and CO_2 (B_c) for the time-varying and snapshot simulations.

in the afternoon, and B_c is relatively constant at 1 through the simulations (data not shown). The entrainment efficiency cannot be assumed equal among the three scalars.

[31] According to equation (4a), the entrainment efficiency of φ can be expressed as

$$B_\varphi = 1 - \frac{1}{2}\frac{\Gamma_{\varphi,2}}{\Gamma_{\varphi,1}}, \tag{6}$$

where $\frac{\delta\varphi_{12}}{\delta h} = 2\Gamma_{\varphi,1}$ is used for the equation derivation. The entrainment efficiency is dependent on the ratio of the vertical gradient of scalar φ in the free atmospheric layer to the inversion jump layer.

[32] So generally, the efficiency is less than unity because the quantity $\frac{\Gamma_{\varphi,2}}{\Gamma_{\varphi,1}}$ is positive. Only when the vertical gradient in the free atmosphere is zero, a condition satisfied for CO_2 in the current time-varying simulations (Figure 10) and for q and CO_2 in the snapshot simulations [*Huang et al.*, 2009, Figure 3], does B_φ approach 1. CO_2 is a well-mixed gas in the free atmosphere. The profile measurement above the ABL [*Lloyd et al.*, 2001; *Górska et al.*, 2008] shows that $\Gamma_{\varphi,2} = 0$ is indeed a good approximation to the real atmospheric flows.

5. Budgets of Heat, Water Vapor, and CO_2 in the ABL

5.1. Budget Equation

[33] Let the square brackets [ ] denote a scalar φ averaged over the depth of the mixed layer

$$[\varphi] = \frac{1}{z_i}\int_0^{z_i} \varphi dz. \tag{7}$$

The mixed layer budget equation can be written as [*Stull*, 1988]

$$\underbrace{z_i \frac{d[\varphi]}{dt}}_{Term\ 1} = \underbrace{\overline{\langle w''\varphi''\rangle_s}}_{Term\ 2} - \underbrace{\overline{\langle w''\varphi''\rangle_i}}_{Term\ 3}, \tag{8}$$

where the covariance terms, $\overline{\langle w''\varphi''\rangle_s}$ and $\overline{\langle w''\varphi''\rangle_i}$ denote domain average and temporal average of the surface flux and the entrainment flux, respectively, of φ at z_i and consist of the sum of both the resolved and subgrid-scale contributions. For the convenience of discussion, $z_i\frac{d[\varphi]}{dt}$ on the left hand side is labeled as Term 1 and $\frac{d[\varphi]}{dt}$ is the time change rate of $[\varphi]$, the surface flux $\overline{\langle w''\varphi''\rangle_s}$ Term 2, and the entrainment flux, $\overline{\langle w''\varphi''\rangle_i}$ Term 3. Equation (8) assumes that horizontal advection is negligible, a condition satisfied in the LES because of the periodic lateral boundary conditions. The net balance between the surface and entrainment fluxes therefore determines any time change in the column-integrated $[\varphi]$.

[34] The three terms in the budget equation are calculated independently. The term $\frac{d[\varphi]}{dt}$ is calculated from the difference between the instantaneous, domain-averaged vertical profiles at the beginning and the end of each hour. Both surface and entrainment fluxes are hourly averages produced by the coupled LES-LSM.

5.2. Budget Analysis

[35] The three terms in equation (8), plotted in Figure 11, show the relative roles of the surface fluxes and the entrainment fluxes in the budgets of the mixed layer potential temperature, water vapor and CO_2. The discussion is limited to the period of 0815 LST to 1615 LST when the ABL experiences appreciable development. The results confirm that the time rate of change in θ, q and c is determined by the difference between their respective vertical fluxes. The surface and entrainment fluxes play different roles in the evolution of the three scalars during the simulation period. In the case of temperature, the temporal change (Term 1) follows closely the surface flux variations (Term 2), confirming that the surface heat flux dominates the evolution of potential temperature in the ABL. In the case of humidity, surface processes transport water vapor from the ground to the mixed layer whereas air entrained from the free atmosphere reduces the specific humidity in the mixed layer. The time change of specific humidity is dependent on the balance of the two fluxes. The entrainment flux is larger than the surface flux in the morning and smaller in the afternoon (see also Figure 5b). As a result, the time rate of change in q is negative in the morning and positive in the afternoon. The ABL mean $\frac{dq}{dt}$, the time change rate of q, is -1.6 g kg^{-1} h^{-1} at 0815 LST and 0.1 g kg^{-1} h^{-1} at 1615 LST. In the case of CO_2, the consumption of the mixed layer CO_2 by photosynthesis at the surface is compensated by the entrainment of air from the free atmospheric layer where the CO_2 mixing ratios are higher. Generally the consumption by photosynthesis exceeds the supply of CO_2 via entrainment. Thus a negative time change of CO_2 in the mixed layer is observed throughout the simulation period.

[36] The relative role of the entrainment in the ABL budget can be further understood through the examination of the ratio of the entrainment to the surface flux over time. As shown in Figure 12, the heat flux ratio A_θ ($\frac{\overline{\langle w''\theta''\rangle_i}}{\overline{\langle w''\theta''\rangle_s}}$, where $\overline{\langle w''\theta''\rangle_i}$ and $\overline{\langle w''\theta''\rangle_s}$ are the LES-resolved entrainment flux at z_i and the surface flux, respectively) is the smallest in magnitude, the water vapor flux ratio A_q (defined as $\frac{\overline{\langle w''q''\rangle_i}}{\overline{\langle w''q''\rangle_s}}$)

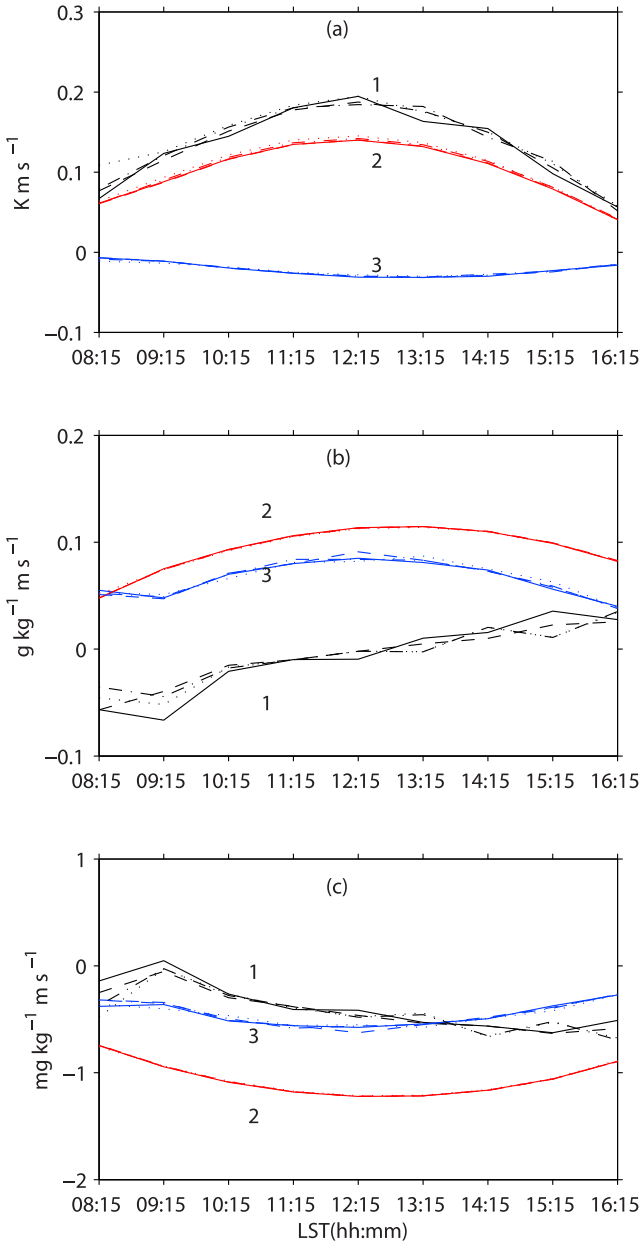

Figure 11. ABL budget of (a) potential temperature, (b) specific humidity, and (c) CO_2 mixing ratio (solid line, u_g = 0 ; dashed line, u_g = 1 m s^{-1}; dash-dotted line, u_g = 3 m s^{-1}; dotted line, u_g = 5 m s^{-1}; 1/black, time rate of change; 2/red, surface flux; 3/blue, entrainment flux).

is the largest, and the CO_2 flux ratio A_c (defined as $\frac{\overline{\langle w''c''\rangle}_i}{\overline{\langle w''c''\rangle}_s}$) lies in between. The entrainment fluxes of these scalars are therefore not a fixed fraction of their surface fluxes, contrary to the assumption often used in ABL models. From aircraft measurements, *Górska et al.* [2008] also found that these three entrainment flux ratios vary significantly with longitude and pointed out their dependence on boundary layer dynamics and surface conditions. These variable flux ratios demonstrate that the entrainment of a scalar depends not only on its surface flux but also on its background profile.

[37] Previously we showed that the surface and entrainment fluxes are insensitive to u_g over the range of u_g values considered (0–5 m s^{-1}). Figure 6 and Table 1 show that the impact of wind speed on the flux ratios is also negligible. In this wind range, flow is still dominated by convection. More differences may be found for higher geostrophic winds (such as 10 to 20 m s^{-1}). *Pino et al.* [2003] found that by changing u_g from 0 to 14 m s^{-1}, the entrainment ratio for temperature changes from the standard value of ~0.25 to 0.3–0.5. *Conzemius and Fedorovich* [2006] showed that at a u_g of 20 m s^{-1}, this ratio can be as large as 1, the exact value

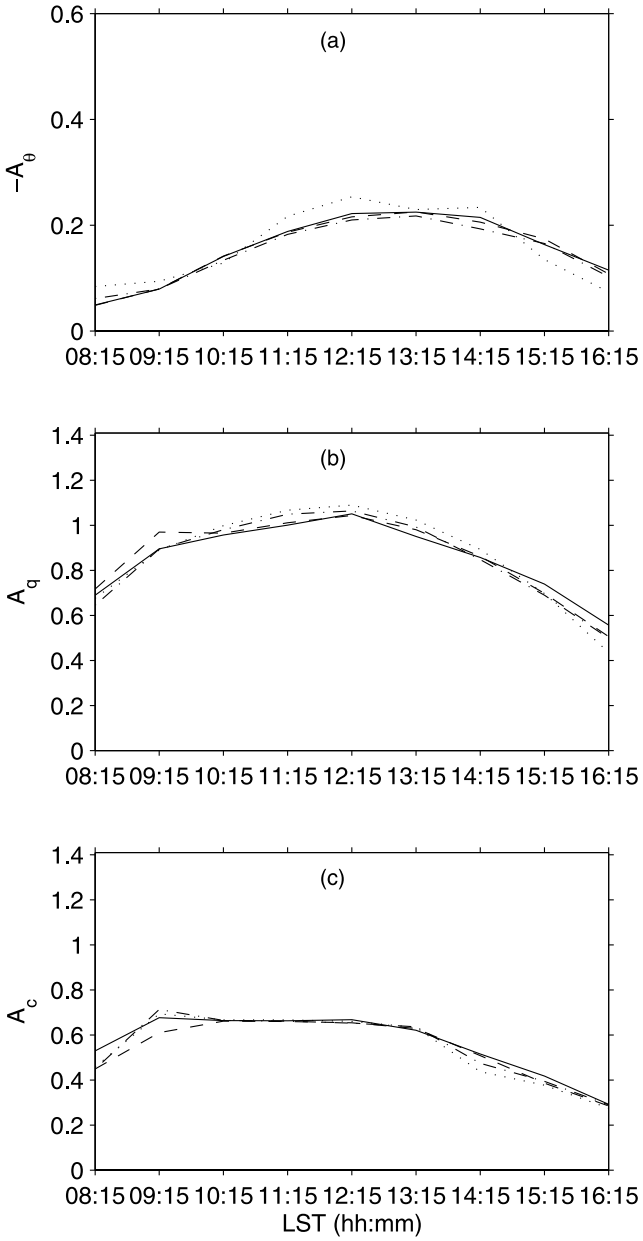

Figure 12. The entrainment-to-surface flux ratio for (a) heat, (b) specific humidity, and (c) CO_2 (solid line, u_g = 0 m s^{-1}; dashed line, u_g = 1 m s^{-1}; dash-dotted line, u_g = 3 m s^{-1}; dotted line, u_g = 5 m s^{-1}).

depending on the wind shear in the boundary layer and the strength of the background stratification.

6. Summary and Conclusions

[38] The domain average surface fluxes of temperature, specific humidity and CO_2 mixing ratio show smooth temporal variations driven by the prescribed variations in the incident solar radiation. At any grid point, the surface sensible and latent heat fluxes fluctuate at high frequencies (seconds to minutes) despite smooth variation of the incoming solar radiation. These fluctuations represent the dynamic response of energy exchange to the heterogeneous turbulent flow in the ABL. In comparison, photosynthesis is insensitive to turbulence for the conditions simulated here.

[39] Scalar entrainment fluxes evolve with time and are not constant fractions of their respective surface fluxes. Examination of the relative entrainment efficiency, the inversion jump, and the exchange coefficients, reveals differences in the entrainment process of the three scalars. The first-order jump model is good approximation for the entrainment fluxes of heat, water vapor and CO_2. The relative entrainment efficiency, determined from the entrainment flux and the local scalar gradient across the capping inversion, is smallest for temperature and largest for CO_2.

[40] The surface and entrainment fluxes play different roles in the time evolution of the three scalars in the daytime ABL. The surface heat flux plays a dominant role in time evolution of potential temperature in the ABL. The time change of the specific humidity depends on the balance of the two fluxes of similar magnitudes. In the case of CO_2, the surface flux usually exceeds the entrainment flux, leading a decreasing trend of CO_2 in the mixed layer through the simulation period.

[41] It is recognized that turbulent organized structures in the ABL are sensitive to the geostrophic wind speed (u_g). In comparison, the mean quantities of the ABL, including the surface and entrainment fluxes, the inversion jump and the time rate of change of the three scalars, are insensitive to the weak to moderate geostrophic forcing discussed here ($u_g \leq 5$ m s^{-1}). For example, increasing u_g from 0 to 5 m s^{-1} increases the surface heat flux by only 3%. However, the influence on entrainment flux and the CBL development can be significant when geostrophic wind is strong [*Conzemius and Fedorovich*, 2006].

[42] **Acknowledgments.** This research was supported by the U.S. Department of Energy's Office of Science (BER) through the Northeastern Regional Center of the National Institute for Climatic Change Research and by the U.S. National Science Foundation through grant ATM-0914473. This research used resources of the National Energy Research Scientific Computing Center, which is supported by the Office of Science of the U.S. Department of Energy under contract DE-AC02-05CH11231. The National Center for Atmospheric Research is sponsored in part by the National Science Foundation.

References

Angevine, W. (1999), Entrainment results including advection and case studies from the Flatland boundary layer experiments, *J. Geophys. Res.*, *104*(D24), 30,947–30,963, doi:10.1029/1999JD900930.

Angevine, W. (2008), Transitional, entraining, cloudy, and coastal boundary layers, *Acta Geophys.*, *56*(1), 2–20, doi:10.2478/s11600-007-0035-1.

Barr, A., and A. Betts (1997), Radiosonde boundary layer budgets above a boreal forest, *J. Geophys. Res.*, *102*(D24), 29,205–29,212, doi:10.1029/97JD01105.

Betts, A. (1973), Non-precipitating cumulus convection and its parameterization, *Q. J. R. Meteorol. Soc.*, *99*(419), 178–196, doi:10.1002/qj.49709941915.

Betts, A. (1974), Reply to comment on the paper "Non-precipitating cumulus convection and its parameterization," *Q. J. R. Meteorol. Soc.*, *100*, 469–471, doi:10.1002/qj.49710042517.

Betts, A. (1992), FIFE atmospheric boundary layer budget methods, *J. Geophys. Res.*, *97*(D17), 18,523–18,531, doi:10.1029/91JD03172.

Betts, A., and J. Ball (1994), Budget analysis of FIFE 1987 Sonde Data, *J. Geophys. Res.*, *99*(D2), 3655–3666, doi:10.1029/93JD02739.

Betts, A., R. Desjardins, J. MacPherson, and R. Kelly (1990), Boundary-layer heat and moisture budgets from FIFE, *Boundary Layer Meteorol.*, *50*(1–4), 109–138, doi:10.1007/BF00120520.

Betts, A., R. Desjardins, and J. MacPherson (1992), Budget analysis of the boundary layer grid flights during FIFE 1987, *J. Geophys. Res.*, *97*(D17), 18,533–18,546, doi:10.1029/91JD03173.

Betts, A. K., B. Helliker, and J. Berry (2004), Coupling between CO_2, water vapor, temperature, and radon and their fluxes in an idealized equilibrium boundary layer over land, *J. Geophys. Res.*, *109*, D18103, doi:10.1029/2003JD004420.

Businger, J., J. Wyngaard, Y. Izumi, and E. Bradley (1971), Flux-profile relationships in the atmospheric surface layer, *J. Atmos. Sci.*, *28*, 181–189, doi:10.1175/1520-0469(1971)028<0181:FPRITA>2.0.CO;2.

Carson, D. (1973), The development of a dry inversion-capped convectively unstable boundary-layer, *Q. J. R. Meteorol. Soc.*, *99*(421), 450–467, doi:10.1002/qj.49709942105.

Chen, J. M., B. Chen, K. Higuchi, J. Liu, D. Chan, D. Worthy, P. Tans, and A. Black (2006), Boreal ecosystems sequestered more carbon in warmer years, *Geophys. Res. Lett.*, *33*, L10803, doi:10.1029/2006GL025919.

Cleugh, H. A., and C. S. B. Grimmond (2001), Modelling regional scale surface energy exchanges and CBL growth in a heterogeneous, urban-rural landscape, *Boundary Layer Meteorol.*, *98*(1), 1–31, doi:10.1023/A:1018798928158.

Conzemius, R. J., and E. Fedorovich (2006), Dynamics of sheared convective boundary layer entrainment, Part I: Methodological background and large-eddy simulations, *J. Appl. Meteorol.*, *63*, 1151–1178.

Deardorff, J. (1979), Prediction of convective mixed-layer entrainment for realistic capping inversion structure, *J. Atmos. Sci.*, *36*, 424–436, doi:10.1175/1520-0469(1979)036<0424:POCMLE>2.0.CO;2.

Deardorff, J. (1980), Stratocumulus-capped mixed layers derived from a 3-dimensional model, *Boundary Layer Meteorol.*, *18*(4), 495–527, doi:10.1007/BF00119502.

Fedorovich, E., R. Conzemius, and D. Mironov (2004), Convective entrainment into a shear-free, linearly stratified atmosphere: Bulk models reevaluated through large eddy simulations, *J. Atmos. Sci.*, *61*(3), 281–295, doi:10.1175/1520-0469(2004)061<0281:CEIASL>2.0.CO;2.

Górska, M., J. V.-G. de Arellano, M. A. Lemone, and C. C. van Heerwaarden (2008), Mean and flux horizontal variability of virtual potential temperature, moisture, and carbon dioxide: Aircraft observations and LES study, *Mon. Weather Rev.*, *136*, 4435–4451.

Grossman, R. (1992), Convective boundary layer budgets of moisture and sensible heat over an unstressed prairie, *J. Geophys. Res.*, *97*(D17), 18,425–18,438, doi:10.1029/92JD01087.

Helliker, B. R., J. A. Berry, A. K. Betts, P. S. Bakwin, K. J. Davis, A. S. Denning, J. R. Ehleringer, J. B. Miller, M. P. Butler, and D. M. Ricciuto (2004), Estimates of net CO_2 flux by application of equilibrium boundary layer concepts to CO_2 and water vapor measurements from a tall tower, *J. Geophys. Res.*, *109*, D20106, doi:10.1029/2004JD004532.

Huang, J., X. Lee, and E. Patton (2008), A modeling study of flux imbalance and the influence of entrainment in the convective boundary layer, *Boundary Layer Meteorol.*, *127*(2), 273–292, doi:10.1007/s10546-007-9254-x.

Huang, J., X. Lee, and E. Patton (2009), Dissimilarity of scalar transport in the convective boundary layer in inhomogeneous landscapes, *Boundary Layer Meteorol.*, *130*(3), 327–345, doi:10.1007/s10546-009-9356-8.

Idso, S. (1981), A set of equations for full spectrum and 8 to 14 μm and 10.5 to 12.5 μm thermal radiation from cloudless skies, *Water Resour. Res.*, *17*(2), 295–304, doi:10.1029/WR017i002p00295.

Klemp, J. B., and D. R. Durran (1983), An upper boundary condition permitting internal gravity wave radiation in numerical mesoscale models, *Mon. Weather Rev.*, *111*, 430–444, doi:10.1175/1520-0493(1983)111<0430:AUBCPI>2.0.CO;2.

Lai, C., A. Schauer, C. Owensby, J. Ham, B. Helliker, P. Tans, and J. Ehleringer (2006), Regional CO_2 fluxes inferred from mixing ratio measurements: Estimates from flask air samples in central Kansas, USA, *Tellus, Ser. B*, *58*, 523–536.

Leuning, R., F. Kelliher, D. De Pury, and E. Schulze (1995), Leaf nitrogen, photosynthesis, conductance and transpiration: Scaling from leaves to canopies, *Plant Cell Environ.*, *18*(10), 1183–1200, doi:10.1111/j.1365-3040.1995.tb00628.x.

Lilly, D. (1968), Models of cloud-topped mixed layers under a strong inversion, *Q. J. R. Meteorol. Soc.*, *94*, 292–309, doi:10.1002/qj.49709440106.

Lloyd, J., et al. (2001), Vertical profiles, boundary layer budgets, and regional flux estimates for CO_2 and Its $^{13}C/^{12}C$ ratio and for water vapor above a forest/bog mosaic in central Siberia, *Global Biogeochem. Cycles*, *15*(2), 267–284, doi:10.1029/1999GB001211.

Moeng, C. (1984), A large-eddy-simulation model for the study of planetary boundary-layer turbulence, *J. Atmos. Sci.*, *41*(13), 2052–2062, doi:10.1175/1520-0469(1984)041<2052:ALESMF>2.0.CO;2.

Patton, E., P. Sullivan, and C. Moeng (2005), The influence of idealized heterogeneity on wet and dry planetary boundary layers coupled to the land surface, *J. Atmos. Sci.*, *62*(7), 2078–2097, doi:10.1175/JAS3465.1.

Pino, D., J. V.-G. de Arellano, and P. G. Duynkerke (2003), The contribution of shear to the evolution of a convective boundary layer, *J. Atmos. Sci.*, *60*(16), 1913–1926, doi:10.1175/1520-0469(2003)060<1913:TCOSTT>2.0.CO;2.

Ronda, R., H. De Bruin, and A. Holtslag (2001), Representation of the canopy conductance in modeling the surface energy budget for low vegetation, *J. Appl. Meteorol.*, *40*(8), 1431–1444, doi:10.1175/1520-0450(2001)040<1431:ROTCCI>2.0.CO;2.

Sorbjan, Z. (1996), Effects caused by varying the strength of the capping inversion based on a large eddy simulation model of the shear-free convective boundary layer, *J. Atmos. Sci.*, *53*(14), 2015–2024, doi:10.1175/1520-0469(1996)053<2015:ECBVTS>2.0.CO;2.

Spalart, P., R. Moser, and M. Rogers (1992), Spectral methods for the Navier-Stokes equations with one infinite and two periodic directions, *J. Comput. Phys.*, *97*, 297–324, doi:10.1016/0021-9991(91)90238-G.

Stull, R. B. (1988), *An Introduction to Boundary Layer Meteorology*, 666 pp., Kluwer Acad., Norwell, Mass.

Sullivan, P., J. McWilliams, and C. Moeng (1996), A grid nesting method for large-eddy simulation of planetary boundary-layer flows, *Boundary Layer Meteorol.*, *80*(1–2), 167–202, doi:10.1007/BF00119016.

Sullivan, P., C. Moeng, B. Stevens, D. Lenschow, and S. Mayor (1998), Structure of the entrainment zone capping the convective atmospheric boundary layer, *J. Atmos. Sci.*, *55*(19), 3042–3064, doi:10.1175/1520-0469(1998)055<3042:SOTEZC>2.0.CO;2.

Sun, J., and Y. Wang (2008), Effect of the entrainment flux ratio on the relationship between entrainment rate and convective Richardson number, *Boundary Layer Meteorol.*, *126*(2), 237–247, doi:10.1007/s10546-007-9231-4.

Tennekes, H. (1973), A model for the dynamics of the inversion above a convective boundary layer, *J. Atmos. Sci.*, *30*(4), 558–567, doi:10.1175/1520-0469(1973)030<0558:AMFTDO>2.0.CO;2.

Vilà-Guerau de Arellano, J. V.-G., B. Gioli, F. Miglietta, H. J. J. Jonker, H. K. Baltink, R. W. A. Hutjes, and A. A. M. Holtslag (2004), Entrainment process of carbon dioxide in the atmospheric boundary layer, *J. Geophys. Res.*, *109*, D18110, doi:10.1029/2004JD004725.

J. Huang, Environmental Modeling Center, NOAA/NCEP, 5200 Auth Rd., Camp Springs, MD 20746, USA. (jianping.huang@noaa.gov)

X. Lee, School of Forestry and Environmental Studies, Yale University, New Haven, CT 06511, USA.

E. G. Patton, Mesoscale and Microscale Meteorology Division, National Center for Atmospheric Research, Boulder, CO 80307, USA.